Robust Locomotion Exploiting Multiple Balance Strategies
An Observer-Based Cascaded Model Predictive Control Approach

Ding, Jiatao; Han, Linyan; Ge, Ligang; Liu, Yizhang; Pang, Jianxin

Robust Locomotion Exploiting Multiple Balance Strategies: An Observer-Based Cascaded Model Predictive Control Approach

Jiatao Ding ⓘ, *Member, IEEE*, Linyan Han ⓘ, Ligang Ge ⓘ, Yizhang Liu ⓘ, and Jianxin Pang ⓘ

Abstract—**Robust locomotion is a challenging task for humanoid robots, especially when considering dynamic disturbances. This article proposes a disturbance observer-based cascaded model predictive control (MPC) approach for bipedal locomotion, with the capability of exploiting ankle, stepping, hip and height variation strategies. Specifically, based on the variable-height inverted pendulum model, a nonlinear MPC that is run at a low frequency is built for 3-D locomotion (i.e., with height variation) while accounting for the footstep modulation as well. Differing from previous works, the nonlinear MPC is formulated as a convex optimization problem by semidefinite relaxation. Subsequently, assuming a flywheel at the pelvis center, a linear MPC that is run at a high frequency is proposed to regulate angular momentum (e.g., through rotating the upper body), which is solved by convex quadratic programming. To run the cascaded MPC in a closed-loop manner, a high order sliding mode observer is designed to estimate system states and dynamic disturbances simultaneously. Simulation and hardware experiments demonstrate the walking robustness in real-world scenarios, including 3-D walking with varying speeds, walking across non-coplanar terrains and push recovery.**

Index Terms—**Bipedal locomotion, convex optimization, disturbance observer, model predictive control, reactive walking.**

I. INTRODUCTION

ROBUST locomotion is a prerequisite for making humanoid robots operate real-world tasks. Tracking the footprints defined in advance, stable walking can be ensured by restricting the center of pressure (CoP) or zero moment point inside the support polygon, which is basically realized through modulating the center of mass (CoM) trajectory or ankle torques, i.e., exploiting the ankle strategy [1]–[3]. For example, one can use the model predictive control (MPC) to attain the optimal CoM trajectory while satisfying feasibility constraints [2]. However, due to the limited foot size, robust locomotion against severe disturbances can not be achieved by merely utilizing the ankle strategy. To enhance the robustness, recent works integrate more balance strategies such as step location modulation (i.e., stepping strategy) [4]–[7], angular momentum adaptation (i.e., hip strategy) [7]–[10], or height variation [10]–[12] in locomotion control.

Among existing algorithms, the MPC has gained a lot of attention due to the following reasons.

1) MPC is naturally formulated as an optimal control problem, which is capable of tackling a large number of constraints.
2) MPC predicts the motion over a horizon, providing a response to dynamic disturbances.
3) MPC can deal with dynamical environments by the receding control mechanism.

For example, based on the linear inverted pendulum (LIP) model, linear model predictive control (LMPC) approaches were developed in [5] and [6] to adjust step locations. Tracking a given height trajectory, [13] built an LMPC for robust walking. Unlike [13] that requires a predefined height trajectory, [14] proposed a nonlinear model predictive control (NMPC) approach for 3-D walking with varying height, with the capability of adjusting the step location. However, angular momentum cannot be modeled by the variable-height inverted pendulum (VHIP) model used in [14]. Based on the nonlinear inverted pendulum plus a flywheel (IPF) model, the authors in [15] proposed another LMPC strategy, which was solved by quadratic programming (QP), to generate 3-D gaits with rotating the upper body. Nevertheless, the stepping strategy was ignored [15]. Although the authors in [16] combined ankle, stepping, and hip strategies, they ignored height variation

To integrate ankle, stepping, hip, and height variation strategies in a unified way, the authors in [17] proposed an LMPC approach where the height trajectory was defined in advance. To alleviate this limitation, [18] proposed an NMPC scheme, which was formulated as a nonconvex quadratically constrained quadratic programming (QCQP) problem. And an enhanced version could be found in [19]. Although the nonconvex QCQP could be solved efficiently by sequential quadratic programming (SQP), the global convergence was hardly guaranteed in [18] and [19].

Another drawback is that most of the above works were only validated by simulations (e.g., [5], [6], [13], [16]–[19]) or run in an open-loop manner (e.g., [14] and [15]), where the problem of state estimation was ignored. In the presence of dynamic disturbances, including modeling errors such as those caused by the usage of a simplified dynamic model (e.g., the LIP model [1]–[3], [20]) and external perturbations such as those caused by external forces, estimating robot states is a nontrivial problem, especially when considering the height variation and the change of angular momentum. To reduce modeling errors, the VHIP model is adopted to account for the height variation (e.g., [14], [21]–[23]) and the IPF model is proposed for characterizing the angular momentum adaptation (e.g., [15], [18], and [24]). Recently, multimass models, such as three-mass LIP [25], [26], have been used to compensate for the mass distribution. Even though, state estimation is dispensable for the closed-loop control.

To this end, the Kalman filter was utilized for estimating CoM state in the 2-D case [27], [28]. Besides, the disturbance-observer-based controller was designed in [29] for locomotion control. To account for the 3-D case with varying height, [30] proposed a dual-loop KF and [31] adopted an extended Kalman filter (EKF) to estimate CoM position and velocity, where the estimation of the angular moment/upper body rotation was ignored. Recent work in [32] proposed a differential dynamic programming approach to estimate 3-D CoM position, linear, and angular momenta, where the speed/accuracy tradeoff needs further investigation.

In this article, we propose a disturbance observer-based MPC scheme for locomotion control, aiming to exploit ankle, stepping, hip, and height variation strategies for maintaining balance. Differing from [17]–[19] that all the four strategies were integrated into one single MPC, this work adopts a two-layer cascaded structure. Specifically, in the first layer, an NMPC, which is formulated as a QCQP, computes 3-D optimal CoM trajectory while modulating the step locations. By semidefinite relaxation (SDR), the nonconvex QCQP is transformed into a convex problem and solved with global convergence. In the second layer, an LMPC, which is solved QP, regulates the angular momentum by rotating the upper body. For the closed-loop control, a high order sliding mode observer (HOSMO) is designed to estimate robot states and dynamic disturbances, based on the nonlinear IPF model.

Compared with existing works, our contributions are
1) Ankle, stepping, hip, and height variation strategies are integrated into a cascaded framework consisting of two MPCs, which are both formulated as convex optimization problems and solved efficiently.
2) The robot states, including 3-D CoM states and 2-D upper body inclination states, as well as the dynamic disturbances are simultaneously estimated by the HOSMO.
3) Robust locomotion in multiple scenarios is realized using the closed-loop MPC scheme, which has been validated by extensive experiments on humanoid robots.

The rest of this article is organized as follows. In Section II, the cascaded MPC is formulated. In Section III, the HOSMO is designed. The experimental results are presented in Section IV. Finally, Section V concludes the article.

II. MPC FORMULATION

To integrate multiple balance strategies for locomotion control without causing a heavy computing burden, this work proposes a two-layer MPC structure, as illustrated in Fig. 1.

A. First-Layer NMPC for 3-D Reactive Locomotion

In this layer, 3-D locomotion with height variation will be tackled, based on the VHIP model. To do this, we manipulate the CoP motion (i.e., employing the ankle strategy) to maintain balance. Meanwhile, the step location is also modulated to reject dynamic disturbances.

1) VHIP Dynamics: Differing from the LIP model [20], the VHIP model can take the vertical motion into consideration [23]. Using VHIP, CoP is computed as

$$p_x = c_x - \frac{c_z - d_z}{g + \ddot{c}_z}\ddot{c}_x, \quad p_y = c_y - \frac{c_z - d_z}{g + \ddot{c}_z}\ddot{c}_y \quad (1)$$

where $[p_x, p_y]^{\mathrm{T}}$, $[c_x, c_y, c_z]^{\mathrm{T}}$, and d_z separately denote the horizontal CoP position, 3-D CoM position and the vertical foot location. $[\ddot{c}_x, \ddot{c}_y, \ddot{c}_z]^{\mathrm{T}}$ denote 3-D CoM acceleration (x, y, and z axis point to the forward, leftward, and the upward direction, respectively) and g is the gravitational acceleration.

2) Cost Function for 3-D Reactive Walking: To accomplish 3-D locomotion following the desired step locations, we start by tracking desired CoM position and step locations. Besides, we regulate the CoM velocity to smooth the trajectory. To reduce the control energy, control inputs (i.e., CoM acceleration) are also penalized. Thus, we have

$$
{}_1f({}_1\boldsymbol{\mathcal{X}}) = \sum_{{}_1\mathbf{X}} \left\{ \frac{\alpha_{{}_1\mathbf{x}}}{2} \parallel {}_1\mathbf{X}_{(k)} - {}_1\mathbf{X}_{(k)}^r \parallel^2 + \frac{\beta_{{}_1\mathbf{x}}}{2} \parallel {}_1\dot{\mathbf{X}}_{(k)} \parallel^2 \right.
$$
$$
\left. + \frac{\gamma_{{}_1\mathbf{x}}}{2} \parallel {}_1\ddot{\mathbf{X}}_{(k)} \parallel^2 \right\}
$$
$$
+ \sum_{\mathbf{D}} \frac{\delta_{\mathbf{D}}}{2} \parallel \mathbf{D}_{(k)} - \mathbf{D}_{(k)}^r \parallel^2 + \sum_{\xi} \frac{\lambda_{\xi}}{2} \parallel \xi \parallel^2 \quad (2)
$$

where $\alpha_{{}_1\mathbf{x}}$, $\beta_{{}_1\mathbf{x}}$, $\gamma_{{}_1\mathbf{x}}$, $\delta_{\mathbf{D}}$, and λ_{ξ} separately denote the penalties to regulate the CoM position, CoM velocity, CoM acceleration, step location, and CoP relaxations. ${}_1\mathbf{X}_{(k)} \in \{\mathbf{C}_{x(k)}, \mathbf{C}_{y(k)}, \mathbf{C}_{z(k)}\}$ represent the predicted CoM position

Fig. 1.   Block diagram of the proposed scheme. $(*)^r$, $(*)^m$, and $(\hat{*})$ separately denote the reference, modulated, and estimated variables.

(e.g., $\mathbf{C}_{x(k)} = [c_{x(k+1)}, \ldots, c_{x(k+N_h)}]^{\mathrm{T}}$ with N_h being the length of prediction horizon) while $_1\mathbf{X}^r_{(k)}$ denotes the reference/desired CoM position. $\mathbf{D}_{(k)} = [d_{(k,1)}, \ldots, d_{(k,N_f)}]^{\mathrm{T}}$ and $\mathbf{D}^r_{(k)} = [d^r_{(k,1)}, \ldots, d^r_{(k,N_f)}]^{\mathrm{T}}$ are the predicted and reference step locations over the horizon ($d \in \{d_x, d_y\}$) [1] with N_f being the number of future step locations over the horizon. CoP relaxation variables ($\xi \in \{\xi_{xl}, \xi_{xu}, \xi_{yl}, \xi_{yu}\}$) are also penalized to suppress CoP deviation.

Using the above cost function (2), the 3-D CoM trajectory and step locations can be modulated in real-time. Particularly, optimal variables $_1\mathcal{X}$ are defined as

$$_1\mathcal{X} = [\ddot{\mathbf{C}}_{x(k)}; \ddot{\mathbf{C}}_{y(k)}; \ddot{\mathbf{C}}_{z(k)}; \mathbf{D}_{x(k)}; \mathbf{D}_{y(k)}; \boldsymbol{\Upsilon}] \quad (3)$$

where $\boldsymbol{\Upsilon} = [\xi_{xl}, \xi_{xu}, \xi_{yl}, \xi_{yu}]^{\mathrm{T}}$ comprise the CoP relaxations.

In this article, reference step locations are defined offline to meet the task requirements, e.g., a walking velocity demand, given a constant step duration. Then, based on LIP, the reference horizontal CoM trajectory is determined by the analytic solution provided in [33]. Besides, the step height is determined by the ground surface profile and the reference CoM height can be computed by linear interpolation [34].

3) Feasibility Constraints for 3-D Reactive Walking: We consider the stability constraints and physical limitations when formulating the NMPC.

a) Slack Constraints on CoP Movement: To guarantee walking stability, CoP should be restricted within the support polygon. Inheriting from [19], we adopt slack constraints

$$\underline{p}_x + \xi_{xl} \le p_{x(k+i)} - d_{x(k+i)} \le \overline{p}_x + \xi_{xu}, i \in \{1, \ldots, N_h\} \quad (4)$$

where $p_{x(k+i)}$ and $d_{x(k+i)}$ denote the x component of CoP and foot location, separately. $\underline{p}_x$ and $\overline{p}_x$ are the lower and upper CoP boundaries, which are determined by the foot size.

Remark 1: One may argue that the slack constraints allow the CoP to deviate from the support region, leading to a fall. However, this could be avoided by setting large penalties, i.e., λ_ξ in (2). On the other hand, even when the generated CoP deviates, the walking stability can still be ensured by making use of the hip strategy, which is realized in the second-layer MPC. In fact, it has been demonstrated that the usage of soft CoP constraints

[1]$[d_{x(k,1)}, \ldots, d_{x(k,N_f)}]^{\mathrm{T}}$ denote the future step locations of different walking cycles falling in the prediction horizon while $[d_{x(k+1)}, \ldots, d_{x(k+N_h)}]^{\mathrm{T}}$ denote step positions at different sampling times over the horizon.

(4) contributes to high solvability (see [19]), which is highly desirable for closed-loop control.

b) Constraints on Stepping Movement: First, kinematic reachability should be obeyed. Taking the step length for example, we have

$$\underline{s}_x \le d_{x(k,j)} - d_{x(k,j-1)} \le \overline{s}_x, \quad j \in \{1, \ldots, N_f\} \quad (5)$$

where $d_{x(k,j)}$ denotes the jth step position over the horizon with $d_{x(k,0)}$ being the current support location, $\underline{s}_x$ and $\overline{s}_x$ are lower and upper boundaries of step length.

Second, the change rate of the swing foot location is limited to respect the actuation capability. In each MPC loop, we add constraints on the next foot location, i.e.,

$$\underline{\dot{d}}_x \Delta t \le d_{x(k,1)} - d_{x(k-1,1)} \le \overline{\dot{d}}_x \Delta t \quad (6)$$

where $d_{x(k-1,1)}$ is the next step location computed by the last MPC loop, $\underline{\dot{d}}_x$ and $\overline{\dot{d}}_x$ are the lower and upper boundaries of the leg velocity, and Δt is the time interval.

c) Constraints on CoM Motion: To avoid an infeasible trajectory that breaks the kinematic limit, the CoM height relative to the support height $d_{z(k+i)}$ is restricted by

$$\underline{h} \le c_{z(k+i)} - d_{z(k+i)} \le \overline{h}, \quad i \in \{1, \ldots, N_h\} \quad (7)$$

where $\underline{h}$ and $\overline{h}$ are the minimal and maximal vertical heights.

Since the ground generates unilateral reactive forces, the CoM acceleration is restricted to avoid a free fall, i.e.,

$$\ddot{c}_{z(k+i)} \ge -g, \quad i \in \{1, \ldots, N_h\}. \quad (8)$$

Consequently, the NMPC scheme is established. Analysis reveals that the feasibility constraints, especially the CoP constraints (4), can be expressed in quadratic forms w.r.t $_1\mathcal{X}$. Therefore, the NMPC is a QCQP problem, see Appendix A1.

Remark 2: Due to the utilization of CoP constraints (4), the above QCQP is a nonconvex problem. Although it can be solved efficiently by SQP, as done in [14], [18], and [19], the global convergence is not guaranteed. Here, we resort to the SDR technique to attain the global optimum, see Appendix A. Although SDR leads to a larger computing burden, the convex transformation enhances the numerical stability, which is crucial to ensure closed-loop performance. Using the *C++* library *Mosek* [35], the NMPC can run at 10 Hz, which is acceptable for locomotion control.

B. Second-Layer LMPC for Angular Momentum Adaptation

The second-layer MPC aims at improving the walking robustness by making use of the hip strategy. To this end, the centroidal moment pivot (CMP), which is defined as the point where a line parallel to the ground reaction force and passing through the CoM intersects the walking surface, is modulated by rotating the upper body [36].

1) IPF Dynamics: Assuming a flywheel at the pelvis center, the change of angular momentum can be characterized by the upper body rotation [24]. Considering the height variation, the nonlinear IPF [34] is used[2], whereby the CMP is

$$\text{cmp}_x = p_x - \dot{L}_y/(m(g + \ddot{c}_z)), \quad \text{with} \quad \dot{L}_y = I_y\ddot{\theta}_p,$$

$$\text{cmp}_y = p_y + \dot{L}_x/(m(g + \ddot{c}_z)), \quad \text{with} \quad \dot{L}_x = I_x\ddot{\theta}_r \quad (9)$$

where $[\text{cmp}_x, \text{cmp}_y]^\text{T}$ denote the CMP position. $[L_x, L_y]^\text{T}$, $[I_x, I_y]^\text{T}$, and $[\theta_r, \theta_p]^\text{T}$ separately denote angular momentum, moment of inertia and upper body rotation angle around x and y axis. $[\ddot{\theta}_r, \ddot{\theta}_p]^\text{T}$ and $[\dot{L}_x, \dot{L}_y]^\text{T}$ denote the angular acceleration of upper body and the change rate of angular momentum. m is the total mass of a robot.

2) Cost Function: At this stage, we track desired body rotation angles while minimizing the angular velocity. To achieve a high walking stability, we expect the CMP to be located at the support center. Furthermore, control inputs (i.e., angular accelerations) are also penalized. As a result, we define

$$_2f(_2\mathcal{X}) = \sum_{_2\mathbf{X}} \left\{ \frac{\alpha_{_2\mathbf{x}}}{2} \parallel {_2\mathbf{X}_{(k)}} - {_2\mathbf{X}^r_{(k)}} \parallel^2 + \frac{\beta_{_2\mathbf{x}}}{2} \parallel {_2\dot{\mathbf{X}}_{(k)}} \parallel^2 \right.$$

$$\left. + \frac{\gamma_{_2\mathbf{x}}}{2} \parallel {_2\ddot{\mathbf{X}}_{(k)}} \parallel^2 \right\}$$

$$+ \sum_{\text{cmp}} \frac{\delta_{\text{cmp}}}{2} \parallel \mathbf{cmp}_{(k)} - \mathbf{cmp}^r_{(k)} \parallel^2 \quad (10)$$

where $_2\mathbf{X} \in \{\boldsymbol{\Theta}_r, \boldsymbol{\Theta}_p\}$ comprise the roll and pitch angles over the prediction horizon, $\mathbf{cmp} \in \{\mathbf{cmp}_x, \mathbf{cmp}_y\}$ consist of the forward and lateral CMP.

By default, the reference body inclination angles $_2\mathbf{X}^r_{(k)}$ are set to be zeros to keep the body upright. To maintain balance, the reference CMP positions coincide with the support centers, generated by the NMPC in Section II-A.

3) Feasibility Constraints: To achieve a feasible motion, CMP motion and the upper body status are constrained.

a) Constraints on CMP Motion: Theoretically, a humanoid robot can maintain balance even though the CMP deviates slightly from the support region [36]. Nevertheless, in this work, we restrict the CMP within the support region, i.e.,

$$\text{cmp}_{x(k+i)} \in \mathbb{S}(d_x), \quad i \in \{1, \ldots, N_x\} \quad (11)$$

---

[2]A three-mass linear IPF model has been proposed in [25]. However, it cannot account for the height variation. Furthermore, a multimass model would cause a heavy computing burden. Thus, we still use the single-mass nonlinear IPF model here, leaving the mass compensation as a future work.

where $\mathbb{S}(d_x)$ represents the support region over the prediction horizon, which is a function of the step location. N_x is the length of the predictive horizon for the LMPC.

Remark 3: Differing from the first-layer MPC where only the single support phase is taken into account when formulating the CoP constraints, the double support phase is also considered here for restricting the CMP motion. During the double support phase, the support region $\mathbb{S}(d_x)$ is the sum of two subzones surrounding two support feet, with each subzone determined by foot size. Certainly, we can equate the CMP (9) with a generalized definition of CoP by taking the body rotation into account. In the following sections, we estimate robot states by taking the measured CoP as CMP.

b) Constraints on Body Rotation: The trunk rotation is restricted to comply with the articulation limit and actuation capability. Taking the roll angle for example, we have

$$\underline{\theta}_r \le \theta_{r(k+i)} \le \overline{\theta}_r, \quad i \in \{1, \ldots, N_x\},$$

$$\underline{\tau}_r \le I_x\ddot{\theta}_{r(k+i)} \le \overline{\tau}_r, \quad i \in \{1, \ldots, N_x\} \quad (12)$$

where $\{\underline{\theta}_r, \overline{\theta}_r\}$ and $\{\underline{\tau}_r, \overline{\tau}_r\}$ are the lower and upper boundaries of roll angle and torque, respectively.

Since CoP position and vertical CoM acceleration in (9) are already generated by the first-layer MPC, the second-layer MPC is only involved with linear constraints. As a result, the LMPC can be formulated as a convex QP problem by tuning weights in (10). Using the off-the-shell QP solver, the second-layer MPC can run at 100 Hz with a 0.05s horizon.

Remark 4: It should be mentioned that we can integrate the hip strategy into the first-layer MPC like [19]. However, it would result in a bigger nonconvex QCQP problem, leading to a much heavier computing burden. Thus, we adopt a cascaded structure here. In this way, two smaller convex optimization problems can be formulated and solved efficiently. Furthermore, using the two-layer structure, the CoP deviation caused by the soft constraints (4) can be compensated by restricting CMP motion, addressing the technique shortcoming in [19].

III. HOSMO-BASED STATE ESTIMATION

For closed-loop control, we propose to use a HOSMO to estimate robot states. Based on the nonlinear IPF dynamics, we estimate the 3-D CoM state, 2-D body inclination state, and dynamic disturbances in all channels simultaneously.

A. Dynamical Model Considering System Uncertainties

Considering the system uncertainties, the dynamical model expressed in (9) can be rewritten as

$$\ddot{c}_x = \frac{c_x - p_x}{m(c_z - d_z)}(f_n + f_z^e) - \frac{\dot{L}_y}{m(c_z - d_z)} + \frac{1}{m}f_x^e + \phi^1_{is}, \quad (13a)$$

$$\ddot{c}_y = \frac{c_y - p_y}{m(c_z - d_z)}(f_n + f_z^e) + \frac{\dot{L}_x}{m(c_z - d_z)} + \frac{1}{m}f_y^e + \phi^2_{is}, \quad (13b)$$

$$\ddot{c}_z = \frac{1}{m}f_n + \frac{1}{m}f_z^e - g + \phi_{is}^3, \tag{13c}$$

$$\ddot{\theta}_p = (\dot{L}_y + \dot{l}_y^e)/I_y + \phi_{is}^4, \tag{13d}$$

$$\ddot{\theta}_r = (\dot{L}_x + \dot{l}_x^e)/I_x + \phi_{is}^5 \tag{13e}$$

where f_n is the vertical ground reactive force, $[f_x^e, f_y^e, f_z^e]^T$, and $[\dot{l}_x^e, \dot{l}_y^e]^T$ separately denotes the external disturbances on CoM motion and the change rate of angular momentum. $[\phi_{is}^1, \phi_{is}^2, \phi_{is}^3, \phi_{is}^4, \phi_{is}^5]^T$ denotes the internal uncertainties including modeling errors.

In practice, internal uncertainties and external disturbances can be regarded as lumped uncertainties. As a result, (13) can be written in a compact form as follows:

$$\ddot{c}_x = f_{cx} + d_{is}^{cx}, \tag{14a}$$

$$\ddot{c}_y = f_{cy} + d_{is}^{cy}, \tag{14b}$$

$$\ddot{c}_z = f_{cz} + d_{is}^{cz}, \tag{14c}$$

$$\ddot{\theta}_p = f_{\theta p} + d_{is}^{\theta p}, \tag{14d}$$

$$\ddot{\theta}_r = f_{\theta r} + d_{is}^{\theta r} \tag{14e}$$

where $[f_{cx}, f_{cy}, f_{cz}, f_{\theta p}, f_{\theta r}]^T$ comprises control inputs that are determined by

$$f_{cx} = ((c_x - p_x)f_n - \dot{L}_y)/(m(c_z - d_z)), \tag{15a}$$

$$f_{cy} = ((c_y - p_y)f_n + \dot{L}_x)/(m(c_z - d_z)), \tag{15b}$$

$$f_{cz} = f_n/m - g, \tag{15c}$$

$$f_{\theta p} = \dot{L}_y/I_y, \tag{15d}$$

$$f_{\theta r} = \dot{L}_x/I_x \tag{15e}$$

and $[\phi_{is}^{cx}, \phi_{is}^{cy}, \phi_{is}^{cz}, \phi_{is}^{\theta p}, \phi_{is}^{\theta r}]^T$ comprises the lumped uncertainties, computed by collecting items on $[f_x^e, f_y^e, f_z^e, \dot{l}_x^e, \dot{l}_y^e]^T$ and $[\phi_{is}^1, \phi_{is}^2, \phi_{is}^3, \phi_{is}^4, \phi_{is}^5]^T$ in (13).

Defining $\mathbf{x}_1 = [c_x, c_y, c_z, \theta_p, \theta_r]^T$, and $\mathbf{x}_2 = \dot{\mathbf{x}}_1$, (14) is

$$\dot{\mathbf{x}}_1 = \mathbf{x}_2,$$

$$\dot{\mathbf{x}}_2 = \mathbf{F} + \mathbf{\Phi}_{is} \tag{16}$$

with $\mathbf{F} = [f_{cx}, f_{cy}, f_{cz}, f_{\theta p}, f_{\theta r}]^T$, $\mathbf{\Phi}_{is} = [\phi_{is}^{cx}, \phi_{is}^{cy}, \phi_{is}^{cz}, \phi_{is}^{\theta p}, \phi_{is}^{\theta r}]^T$.

B. HOSMO Formulation

Let us define the operators on a vector $\boldsymbol{\kappa} \in \Re^N$ as follows:

$$\mathbf{sig}^\rho(\boldsymbol{\kappa}) = [|\kappa_1|^\rho \mathrm{sign}(\kappa_1), |\kappa_2|^\rho \mathrm{sign}(\kappa_2), \ldots, |\kappa_N|^\rho \mathrm{sign}(\kappa_N)]^T,$$

$$\mathbf{sign}(\boldsymbol{\kappa}) = [\mathrm{sign}(\boldsymbol{\kappa}_1), \mathrm{sign}(\boldsymbol{\kappa}_2), \ldots, \mathrm{sign}(\boldsymbol{\kappa}_N)]^T,$$

$$\mathbf{diag}(\boldsymbol{\kappa}) = \mathrm{diag}[\kappa_1, \kappa_2, \ldots, \kappa_N],$$

$$(\boldsymbol{\kappa})^\rho = [(\boldsymbol{\kappa}_1)^\rho, (\boldsymbol{\kappa}_2)^\rho, \ldots, (\boldsymbol{\kappa}_N)^\rho]^T \tag{17}$$

where $\mathrm{sign}()$ denotes the signum function, and $\mathrm{diag}()$ is the function that produces a diagonal matrix.

The system states and lumped disturbances in (16) are estimated by HOSMO [37], which is designed as

$$\dot{\hat{\mathbf{x}}}_1 = \hat{\mathbf{x}}_2 + \mathbf{diag}(\mathbf{L}_1)\mathbf{sig}^{\frac{2}{3}}(\mathbf{x}_1 - \hat{\mathbf{x}}_1),$$

$$\dot{\hat{\mathbf{x}}}_2 = \mathbf{F} + \hat{\mathbf{\Phi}}_{is} + \mathbf{diag}(\mathbf{L}_2)\mathbf{sig}^{\frac{1}{3}}(\mathbf{x}_1 - \hat{\mathbf{x}}_1),$$

$$\dot{\hat{\mathbf{\Phi}}}_{is} = \mathbf{diag}(\mathbf{L}_3)\mathbf{sign}(\mathbf{x}_1 - \hat{\mathbf{x}}_1) \tag{18}$$

where $\hat{\mathbf{x}}_1$, $\hat{\mathbf{x}}_2$, and $\hat{\mathbf{\Phi}}_{is}$ are the estimation results of $\mathbf{x}_1$, $\mathbf{x}_2$, and $\mathbf{\Phi}_{is}$, respectively. $\mathbf{L}_1 \in \Re^5$, $\mathbf{L}_2 \in \Re^5$, and $\mathbf{L}_3 \in \Re^5$ are gains.

In this work, we bound the lumped uncertainties by

$$|\dot{\mathbf{\Phi}}_{is(i)}| \le \mathbf{\Delta}_{(i)}, \quad i = 1, 2, \ldots 5 \tag{19}$$

where $\mathbf{\Delta} \in \Re^5$ consists of the boundary values of the change rates of system uncertainties.

Then, gains of HOSMO are determined by

$$\mathbf{L}_1 = \mu_1(\mathbf{\Delta}^{\frac{1}{3}}),$$

$$\mathbf{L}_2 = \mu_2 \mu_1^{\frac{1}{2}}(\mathbf{\Delta}^{\frac{2}{3}}),$$

$$\mathbf{L}_3 = \mu_3(\mathbf{\Delta}) \tag{20}$$

where μ_1, μ_2, and μ_3 are the selected real numbers.

As a result, a nonlinear disturbance observer for states and disturbances estimation is established. The error analysis can be found in Appendix B.

IV. EXPERIMENTS

To verify the walking robustness, we conduct extensive experiments on humanoid robots, including dynamic simulations on the COMAN robot [38] and hardware experiments on the Walker2 robot [39].

A. Dynamic Simulations on the COMAN Robot

Dynamic simulations in real-world scenarios including walking across a low passage and push recovery have been conducted on the COMAN robot, which can be found in the attached video. For the sake of brevity, the push recovery test is presented here, where the horizontal forces were separately applied to the pelvis over $3.4-3.5$ s (forward 220 N, leftward 110 N) and $6.6-6.7$ s (backward 220 N, rightward 60 N) when the robot was stepping in place.

1) State Estimation Performance: The boundaries of system disturbances and the coefficients used for the HOSMO are

$$\mathbf{\Delta} = [250, 200, 200, 150, 150]^T,$$

$$\boldsymbol{\sigma} = [2.5, 2, 0.5]^T. \tag{21}$$

The state-of-the-art EKF scheme proposed in [31] is used as a comparison, which estimates 3-D CoM position, CoM velocity, and external forces based on the VHIP model. The covariance matrices of the EKF are

$$Q = \mathrm{diag}[5e - 6\mathbf{I}, 5e - 4\mathbf{I}, 3e\mathbf{I}],$$

$$R = \mathrm{diag}[5e - 6\mathbf{I}, 1e - 4\mathbf{I}] \tag{22}$$

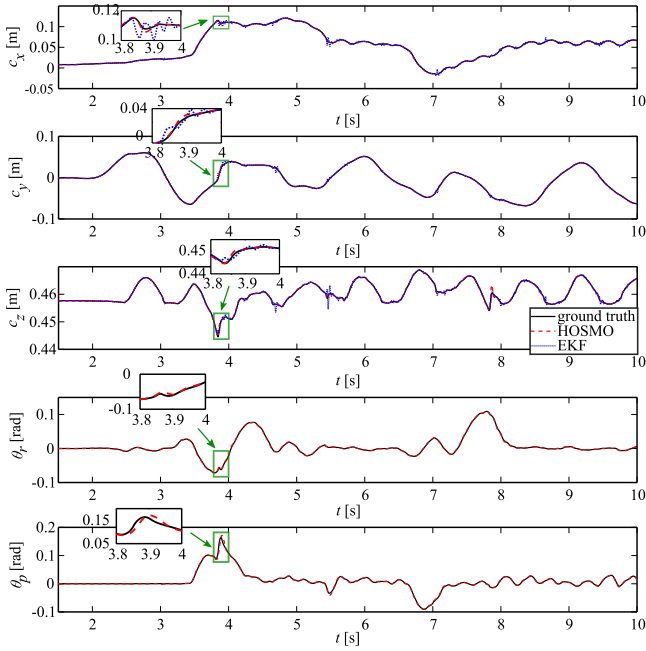where $\mathbf{I} \in \Re^{3 \times 3}$ is the identity matrix.

This article has been accepted for inclusion in a future issue of this journal. Content is final as presented, with the exception of pagination.

6   IEEE/ASME TRANSACTIONS ON MECHATRONICS

Fig. 2.   CoM position and upper body rotation angle for push recovery.

Fig. 3.   Lumped system uncertainties for push recovery.

TABLE I
RMSE VALUES OF ESTIMATED STATES

	c_x[m]	c_y[m]	c_z[m]	θ_r[rad]	θ_p[rad]
HOSMO	0.00040	0.00062	0.00023	0.00091	0.0019
EKF	0.0012	0.0011	0.00032	-	-
	$\dot{c}_x$[m/s]	$\dot{c}_y$[m/s]	$\dot{c}_z$[m/s]	$\dot{\theta}_r$[rad/s]	$\dot{\theta}_p$[rad/s]
HOSMO	0.019	0.018	0.018	0.073	0.11
EKF	0.025	0.023	0.022	-	-

TABLE II
MODULATED STEP PARAMETERS FOR PUSH RECOVERY

Paras \ step	4	5	6	7	8	9	10	11
s_x [cm]	7.9	0.6	-8.5	0.5	-3.5	3.0	0.07	-0.07
s_y [cm]	14.54	14.50	14.52	-	-	-	-	-

In Fig. 2, CoM positions estimated by the HOSMO are almost overlapped by the ground truth, especially when compared with results obtained by the EKF (see the partially enlarged drawings). Numerical analysis (see Table I) reveals that the HOSMO contributes to smaller root mean square errors (RMSEs) than the EKF. Besides, upper body rotation angles can be estimated by the proposed HOSMO, which are ignored in [31]. The plots in Fig. 2 and RMSEs listed in Table I indicate that the estimated angles are accurate enough.

The CoM velocity and upper body angular velocity are also estimated by the HOSMO. As listed in Table I, the HOSMO generates smaller RSMEs of the CoM velocity than the EKF.

The estimated system disturbances are illustrated in Fig. 3. As can be seen from the partially enlarged drawings, the HOSMO results in a shorter time delay than the EKF, meaning a faster convergence. It should be mentioned that there exist quasi-periodic jerks in 3-D CoM channels when using the EKF approach, caused by the landing impact. In contrast, since we consider the rotation of the upper body, the estimated F^es are smoothed using the HOSMO. One may notice that there are estimation errors in the lateral push forces (see enlarged drawings on F_y^e), which can be explained by the fact that HOSMO estimated lumped disturbances, reflecting the accumulative effect of the internal uncertainty and the external pushes. And, the estimated torques,
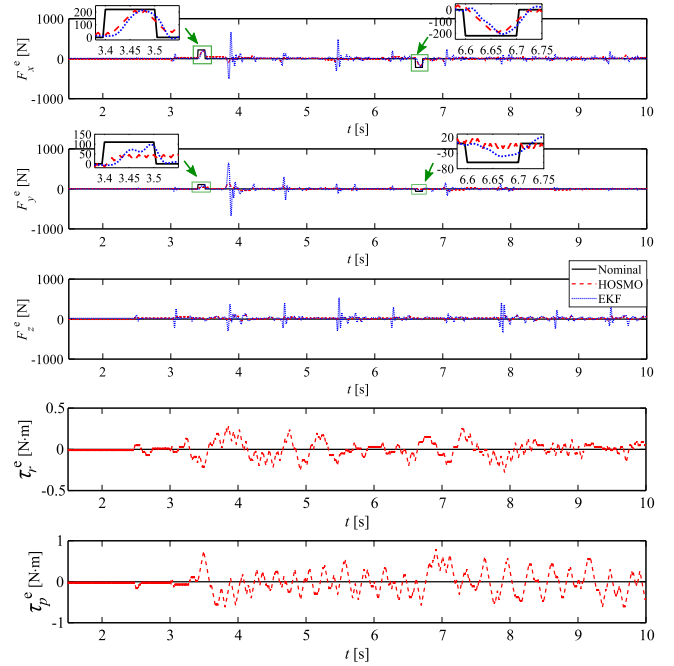
i.e., τ_p^e and τ_r^e, account for the internal uncertainties including modeling errors.

2) Push Recovery Performance: As can be seen in Fig. 2, the robot adjusted CoM height and the upper body rotation angles to accommodate external pushes. For example, when the forward push is applied over 3.4–3.5 s, the robot reduces the CoM height and leans forward simultaneously to reconcile with the push force. Namely, the hip and height variation strategies are enabled for push recovery.
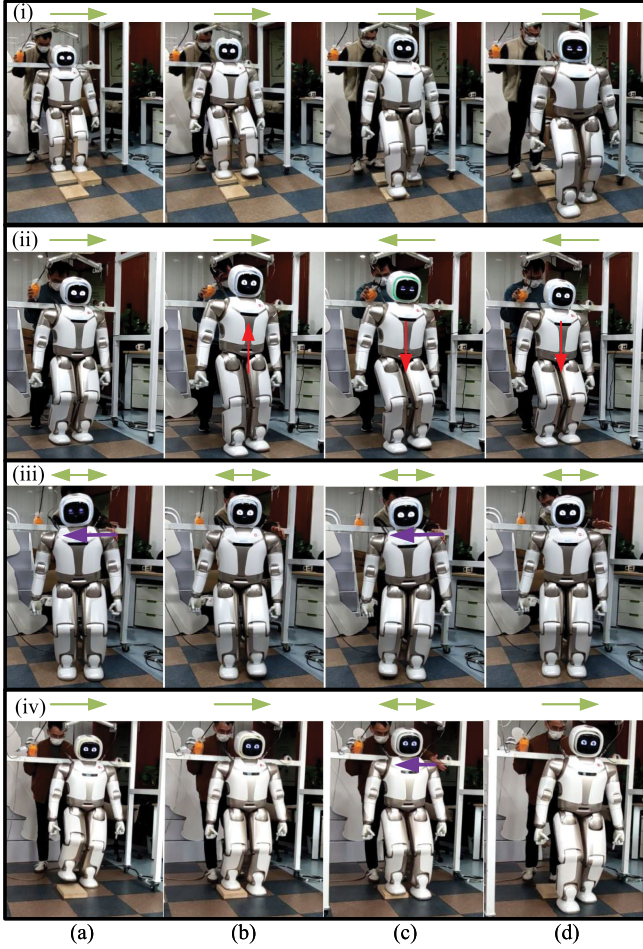
Another phenomenon is that the step length (s_x, by default is 0 cm) is modulated in real-time, as listed in Table II. As a result, the robot could adjust the support region to reject push forces. Since the lateral push is small, which can be rejected by the hip and height variation strategies, the step width (s_y, by default is 14.52 cm) does not change a lot. After the 6th step, the step width coincides with the default one.

A comparative study shows that the robot falls when the open-loop MPC is used. Please check the supplementary video for more details.

B. Hardware Experiments on the Walker2 Robot

Hardware experiments are conducted on the Walker2 robot. It turns out that the robot equipped with the closed-loop MPC scheme can walk stably in various scenarios (see the attached
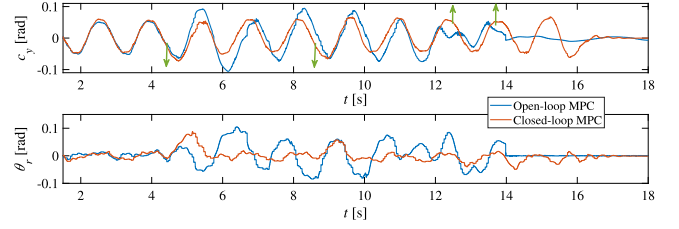
This article has been accepted for inclusion in a future issue of this journal. Content is final as presented, with the exception of pagination.

DING *et al.*: ROBUST LOCOMOTION EXPLOITING MULTIPLE BALANCE STRATEGIES
7

Fig. 5. Robot motions under external pushes when using the open-loop/closed-loop MPC approach. Note that only the first rightward force was applied when using the open-loop MPC whereas multiple pushes are applied when using the closed-loop MPC. Vertical arrows mark the force directions.

Fig. 4. Walker2 walks stably in real-world scenarios. (i) Stable walking across non-coplanar terrains. (ii) 3-D walking with varying directions. (iii) Push recovery when stepping in place. (iv) Push recovery when stepping on a stone. Horizontal arrows above each arrow mark waking directions with the right and left arrows separately marking the forward and backward walking. The bidirectional arrows indicate the robot is stepping in place. The upward and downward arrows in the (ii)-row indicate the robot is walking with the stretching and bending leg, respectively. The horizontal arrows (points to the left direction) in the (iii)-row and (iv)-row mark the external push forces "The horizontal arrows in the (iii)-row and (iv)-row mark the external push forces.

video). Fig. 4 shows the snapshots of walking across non-coplanar terrains [(i)-row], 3-D walking with varying directions [(ii)-row], push recovery when stepping in place [(iii)-row] and push recovery when stepping on a stone [(iv)-row].

Here, we present the push recovery in detail. When the robot was stepping in place, lateral push forces were applied to the shoulder [see the (iii)-row]. Fig. 5 illustrated the resultant lateral CoM trajectories and roll angles. As can be seen from Fig. 5, when the rightward force was applied, the open-loop MPC would generate huge fluctuation without returning to a normal gait. On the contrary, the closed-loop MPC contributes to a fast recovery. Furthermore, the closed-loop strategy helps to reject multiple push forces from different directions.

A more challenging task can be found in the (iv)-row, where lateral pushes were applied when stepping on a stone. In this

case, the step location modulation and CoM variation are both limited due to the non-coplanar terrain. To tackle this issue, we chose large $\alpha_{1\mathbf{x}}$, and δ_{D} in (2). Namely, the stepping and height variation strategies were not used. Even though, the robot maintained balance by rotating the upper body. That is, the single-mass nonlinear IPF used in the second-layer MPC helps to enhance the robustness. Also, this experiment demonstrates that the cascaded strategy can run flexibly to achieve robust locomotion in a challenging scenario.

V. CONCLUSION

In this article, we propose a cascaded MPC framework for robust locomotion, which is capable of combing ankle, stepping, hip, and height variation strategies. Using this framework, the footstep modulation and height variation are tackled by solving a QCQP and the angular momentum adaptation is realized by solving a QP. Due to the cascaded structure, two convex optimization problems are solved with high time efficiency. To improve the closed-loop performance, a HOSMO is designed for states and disturbances estimation. Consequently, extensive experiments demonstrate the walking robustness against external pushes. Furthermore, the robot equipped with the approach can accomplish challenging tasks, such as 3-D walking with height variation and walking across non-coplanar terrains.

Our work can be improved by: 1) employing a multimass model to account for the leg dynamics; and 2) adjusting step timing to further enhance the robustness.

APPENDIX A
QCQP FORMULATION AND SOLUTION

A. Nonconvex QCQP

Using the prediction model given in [19], the first-layer NMPC is be formulated as a QCQP problem, expressed as

$$\min_{_1\boldsymbol{\mathcal{X}}} \quad _1f(_1\boldsymbol{\mathcal{X}}) = {}_1\boldsymbol{\mathcal{X}}^{\mathrm{T}}\mathbf{G}(_1\boldsymbol{\mathcal{X}}) + \mathbf{g}^{\mathrm{T}}{}_1\boldsymbol{\mathcal{X}},$$

$$\text{s.t.} \quad h_j(_1\boldsymbol{\mathcal{X}}) \leq 0,$$

$$h_j(_1\boldsymbol{\mathcal{X}}) = {}_1\boldsymbol{\mathcal{X}}^{\mathrm{T}}\mathbf{V}_j(_1\boldsymbol{\mathcal{X}}) + \mathbf{v}_j^{\mathrm{T}}(_1\boldsymbol{\mathcal{X}}) + \sigma_j, j \in \{1,\ldots,N_c\}$$

$$(23)$$

where $\mathbf{G}$, $\mathbf{V}_j \in \Re^{N_t \times N_t}$, $\mathbf{g}$, $\mathbf{v}_j \in \Re^{N_t}$, and $\sigma_j \in \Re$ are the parameters that specify the objective function and constraints, N_c is the number of constraints.

Using the prediction model in [19], quadratic expressions of the constraints, especially the CoP constraints (4) can be derived, which are omitted for the sake of brevity.

B Semidefinite Relaxation for QCQP Solution

The nonconvex QCQP problem can be transformed into a convex problem using the SDR technique [40]. By introducing $x_t \in \Re$ ($x_t{}^2 = 1$), we can homogenize (23) as

$$\min_{\mathbf{_1\mathcal{X}},\ x_t} \quad \begin{bmatrix} _1\mathcal{X}^{\mathrm{T}} & x_t \end{bmatrix} \begin{bmatrix} \mathbf{G} & \mathbf{g} \\ \mathbf{g}^{\mathrm{T}} & 0 \end{bmatrix} \begin{bmatrix} _1\mathcal{X} \\ x_t \end{bmatrix},$$

$$\text{s.t.} \quad \begin{bmatrix} _1\mathcal{X}^{\mathrm{T}} & x_t \end{bmatrix} \begin{bmatrix} \mathbf{V}_j & \mathbf{v}_j \\ \mathbf{v}_j^{\mathrm{T}} & 0 \end{bmatrix} \begin{bmatrix} _1\mathcal{X} \\ x_t \end{bmatrix} \le \sigma_j,$$

$$x_t^2 = 1. \tag{24}$$

Let $\mathcal{S}^n$ denote the space of real symmetric $n \times n$ matrices. By introducing the new variable $\bar{\mathcal{X}} = [_1\mathcal{X}^{\mathrm{T}}, x_t]^{\mathrm{T}}$, the problem given by (24) can be organized in the following form:

$$\min_{\bar{\mathcal{X}}} \quad \bar{\mathcal{X}}^{\mathrm{T}} M_0 \bar{\mathcal{X}},$$

$$\text{s.t.} \quad \bar{\mathcal{X}}^{\mathrm{T}} M_j \bar{\mathcal{X}} \le \sigma_j, \quad \bar{\mathcal{X}}^{\mathrm{T}} M_{(N_c+1)} \bar{\mathcal{X}} = 1 \tag{25}$$

where M_0, M_{N_c+1}, and M_j ($1 \le j \le N_c$) are members of $\mathcal{S}^{N_t+1}$, which are defined as

$$M_0 = \begin{bmatrix} \mathbf{G} & \mathbf{g} \\ \mathbf{g}^{\mathrm{T}} & 0 \end{bmatrix}, \quad M_j = \begin{bmatrix} \mathbf{V}_j & \mathbf{v}_j \\ \mathbf{v}_j^{\mathrm{T}} & 0 \end{bmatrix}, \quad M_{(N_c+1)} = \begin{bmatrix} \mathbf{0} & \mathbf{0} \\ \mathbf{0} & 1 \end{bmatrix}. \tag{26}$$

By introducing $X = \bar{\mathcal{X}}\bar{\mathcal{X}}^{\mathrm{T}}$, we can observe that

$$\bar{\mathcal{X}}^{\mathrm{T}} M \bar{\mathcal{X}} = \text{tr}(M\bar{\mathcal{X}}\bar{\mathcal{X}}^{\mathrm{T}}) = M \bullet X \tag{27}$$

where $M \bullet X = \sum_i \sum_j M_{ij} X_{ij}$ represents the inner product operation of M and X.

Note that X is a rank one symmetric positive semidefinite matrix. As a result, the problem (25) is transferred as

$$\min_{X} \quad M_0 \bullet X,$$

$$\text{s.t.} \quad M_j \bullet X \le \sigma_j, \quad M_{N_c+1} \bullet X = 1,$$

$$X \succeq \mathbf{0}, \quad \text{rank}(X) = 1. \tag{28}$$

Here, we use $X \succeq \mathbf{0}$ to indicate that X is positive semidefinite.

By dropping the rank one constraint on X in problem (28), the primal SDP problem in an inequality form is obtained, whose global optimum can be obtained by off-the-shelf solvers, such as SDPT3 and Sedumi. In this work, we use the *Mosek* library to solve this problem.

APPENDIX B
ERROR DYNAMICS OF HOSMO

Defining estimation errors as $\mathbf{e}_1 = \mathbf{x}_1 - \hat{\mathbf{x}}_1$, $\mathbf{e}_2 = \mathbf{x}_2 - \hat{\mathbf{x}}_2$, and $\mathbf{e}_3 = \mathbf{D}_{is} - \hat{\mathbf{D}}_{is}$, the error dynamics are derivated as

$$\dot{\mathbf{e}}_1 = \mathbf{e}_2 - \mathbf{diag}(\mathbf{L}_1)\mathbf{sig}^{\frac{2}{3}}(\mathbf{e}_1),$$

$$\dot{\mathbf{e}}_2 = \mathbf{e}_3 - \mathbf{diag}(\mathbf{L}_2)\mathbf{sig}^{\frac{1}{3}}(\mathbf{e}_1),$$

$$\dot{\mathbf{e}}_3 = -\mathbf{diag}(\mathbf{L}_3)\mathbf{sig}^{\frac{2}{3}}(\mathbf{e}_1) + \dot{\mathbf{D}}_{is}. \tag{29}$$

Considering (17), the error system (29) can be rewritten as

$$\dot{\mathbf{e}}_1 = \mathbf{e}_2 - \mu_1 \Xi^{\frac{1}{3}}\mathbf{sig}^{\frac{2}{3}}(\mathbf{e}_1),$$

$$\dot{\mathbf{e}}_2 = \mathbf{e}_3 - \mu_2 \Xi^{\frac{1}{2}}\mathbf{sig}^{\frac{1}{2}}(\mathbf{e}_2 - \dot{\mathbf{e}}_1),$$

$$\dot{\mathbf{e}}_3 = -\mu_3 \Xi\,\mathbf{sign}(\mathbf{e}_3 - \dot{\mathbf{e}}_2) + \dot{\mathbf{D}}_{is} \tag{30}$$

where $\Xi = \mathbf{diag}(\Delta)$.

According to [37], we can prove that the system (30) is finite-time convergent by selecting the proper parameters, i.e., μ_1, μ_2, and μ_3. The proof is ignored here.

REFERENCES

[1] S. Kajita *et al.*, "Biped walking pattern generation by using preview control of zero-moment point," in *Proc. IEEE Int. Conf. Robot. Autom.*, 2003, vol. 2, pp. 1620–1626.

[2] P.-B. Wieber, "Trajectory free linear model predictive control for stable walking in the presence of strong perturbations," in *Proc. IEEE-RAS Int. Conf. Humanoid Robots*, 2006, pp. 137–142.

[3] Y.-D. Hong and J.-H. Kim, "3-D command state-based modifiable bipedal walking on uneven terrain," *IEEE/ASME Trans. Mech.*, vol. 18, no. 2, pp. 657–663, Apr. 2013.

[4] Y.-D. Hong and B. Lee, "Real-time feasible footstep planning for bipedal robots in three-dimensional environments using particle swarm optimization," *IEEE/ASME Trans. Mech.*, vol. 25, no. 1, pp. 429–437, Feb. 2020.

[5] A. Herdt, H. Diedam, P.-B. Wieber, D. Dimitrov, K. Mombaur, and M. Diehl, "Online walking motion generation with automatic footstep placement," *Adv. Robot.*, vol. 24, no. 5–6, pp. 719–737, Apr. 2010.

[6] M. Khadiv, A. Herzog, S. A. A. Moosavian, and L. Righetti, "Walking control based on step timing adaptation," *IEEE Trans. Robot.*, vol. 36, no. 3, pp. 629–643, Jun. 2020.

[7] H. Jeong, I. Lee, J. Oh, K. K. Lee, and J.-H. Oh, "A robust walking controller based on online optimization of ankle, hip, and stepping strategies," *IEEE Trans. Robot.*, vol. 35, no. 6, pp. 1367–1386, Dec. 2019.

[8] R. Schuller, G. Mesesan, J. Englsberger, J. Lee, and C. Ott, "Online centroidal angular momentum reference generation and motion optimization for humanoid push recovery," *IEEE Robot. Autom. Lett.*, vol. 6, no. 3, pp. 5689–5696, Jul. 2021.

[9] Z. Zhang, J. Yan, X. Kong, G. Zai, and Y. T. Liu, "Efficient motion planning based on kinodynamic model for quadruped robots following persons in confined spaces," *IEEE/ASME Trans. Mech.*, vol. 26, no. 4, pp. 1997–2006, Aug. 2021.

[10] J. Englsberger and C. Ott, "Integration of vertical COM motion and angular momentum in an extended capture point tracking controller for bipedal walking," in *Proc. IEEE-RAS Int. Conf. Humanoid Robots*, 2012, pp. 183–189.

[11] J. Liu, H. Chen, P. M. Wensing, and W. Zhang, "Instantaneous capture input for balancing the variable height inverted pendulum," *IEEE Robot. Autom. Lett.*, vol. 6, no. 4, pp. 7421–7428, Jul. 2021.

[12] B. J. Van Hofslot, R. Griffin, S. Bertrand, and J. Pratt, "Balancing using vertical center-of-mass motion: A 2-D analysis from model to robot," *IEEE Robot. Autom. Lett.*, vol. 4, no. 4, pp. 3247–3254, Oct. 2019.

[13] J. Lack, "Integrating the effects of angular momentum and changing center of mass height in bipedal locomotion planning," in *Proc. IEEE-RAS Int. Conf. Humanoid Robots*, 2015, pp. 651–656.

This article has been accepted for inclusion in a future issue of this journal. Content is final as presented, with the exception of pagination.

DING *et al.*: ROBUST LOCOMOTION EXPLOITING MULTIPLE BALANCE STRATEGIES 9

[14] K. Van Heerden, "Real-time variable center of mass height trajectory planning for humanoids robots," *IEEE Robot. Autom. Lett.*, vol. 2, no. 1, pp. 135–142, Jun. 2017.

[15] K. Guan, K. Yamamoto, and Y. Nakamura, "Virtual-mass-ellipsoid inverted pendulum model and its applications to 3D bipedal locomotion on uneven terrains," in *Proc. IEEE/RSJ Int. Conf. Intell. Robot. Syst.*, 2019, pp. 1401–1406.

[16] Z. Aftab, T. Robert, and P.-B. Wieber, "Ankle, hip and stepping strategies for humanoid balance recovery with a single model predictive control scheme," in *Proc. IEEE-RAS Int. Conf. Humanoid Robots*, 2012, pp. 159–164.

[17] M. Shafiee-Ashtiani, A. Yousefi-Koma, and M. Shariat-Panahi, "Robust bipedal locomotion control based on model predictive control and divergent component of motion," in *Proc. IEEE Int. Conf. Robot. Autom.*, 2017, pp. 3505–3510.

[18] J. Ding, C. Zhou, S. Xin, X. Xiao, and N. Tsagarakis, "Nonlinear model predictive control for robust bipedal locomotion: Exploring angular momentum and com height changes," *Adv. Robot.*, vol. 35, no. 18, pp. 1079–1097, Aug. 2021.

[19] J. Ding, S. Xin, T. L. Lam, and S. Vijayakumar, "Versatile locomotion by integrating ankle, hip, stepping, and height variation strategies," in *Proc. IEEE Int. Conf. Robot. Autom.*, 2021, pp. 2957–2963.

[20] S. Kajita, F. Kanehiro, K. Kaneko, K. Yokoi, and H. Hirukawa, "The 3D linear inverted pendulum mode: A simple modeling for a biped walking pattern generation," in *Proc. IEEE/RSJ Int. Conf. Intell. Robot. Syst.*, 2001, vol. 1, pp. 239–246.

[21] S. Caron, A. Escande, L. Lanari, and B. Mallein, "Capturability-based pattern generation for walking with variable height," *IEEE Trans. Robot.*, vol. 36, no. 2, pp. 517–536, Apr. 2020.

[22] A. Pajon and P.-B. Wieber, "Safe 3D bipedal walking through linear MPC with 3D capturability," in *Proc. IEEE Int. Conf. Robot. Autom.*, 2019, pp. 1404–1409.

[23] M. A. Hopkins, D. W. Hong, and A. Leonessa, "Humanoid locomotion on uneven terrain using the time-varying divergent component of motion," in *Proc. IEEE-RAS Int. Conf. Humanoid Robots*, 2014, pp. 266–272.

[24] J. Pratt, J. Carff, S. Drakunov, and A. Goswami, "Capture point: A step toward humanoid push recovery," in *Proc. IEEE-RAS Int. Conf. Humanoid Robots*, 2006, pp. 200–207.

[25] R. C. Luo and C. C. Chen, "Biped walking trajectory generator based on three-mass with angular momentum model using model predictive control," *IEEE Trans. Ind. Electron.*, vol. 63, no. 1, pp. 268–276, Jan. 2016.

[26] S. Shimmyo, T. Sato, and K. Ohnishi, "Biped walking pattern generation by using preview control based on three-mass model," *IEEE Trans. Ind. Electron.*, vol. 60, no. 11, pp. 5137–5147, Nov. 2013.

[27] B. J. Stephens, "State estimation for force-controlled humanoid balance using simple models in the presence of modeling error," in *Proc. IEEE Int. Conf. Robot. Autom.*, 2011, pp. 3994–3999.

[28] R. Wittmann, A.-C. Hildebrandt, D. Wahrmann, D. Rixen, and T. Buschmann, "State estimation for biped robots using multibody dynamics," in *Proc. IEEE/RSJ Int. Conf. Intell. Robot. Syst.*, 2015, pp. 2166–2172.

[29] B.-K. Cho, D. Ahn, Y. Jun, and P. Oh, "A posture balance controller for a humanoid robot using state and disturbance-observer-based state feedback," *J. Intell. Robot. Syst.*, vol. 95, no. 2, pp. 331–349, Aug. 2019.

[30] H. Bae, H. Jeong, J. Oh, K. Lee, and J.-H. Oh, "Humanoid robot com kinematics estimation based on compliant inverted pendulum model and robust state estimator," in *Proc. IEEE/RSJ Int. Conf. Intell. Robot. Syst.*, 2018, pp. 747–753.

[31] S. Piperakis, M. Koskinopoulou, and P. Trahanias, "Nonlinear state estimation for humanoid robot walking," *IEEE Robot. Autom. Lett.*, vol. 3, no. 4, pp. 3347–3354, Oct. 2018.

[32] F. Bailly, J. Carpentier, and P. Souères, "Optimal estimation of the centroidal dynamics of legged robots," in *Proc. IEEE Int. Conf. Robot. Autom.*, 2021, pp. 4912–4918.

[33] J. Ding, C. Zhou, Z. Guo, X. Xiao, and N. Tsagarakis, "Versatile reactive bipedal locomotion planning through hierarchical optimization," in *Proc. IEEE Int. Conf. Robot. Autom.*, 2019, pp. 256–262.

[34] S. Kajita, H. Hirukawa, K. Harada, and K. Yokoi, *Introduction to Humanoid Robotics*, vol. 101. Berlin, Germany: Springer, 2014.

[35] M. ApS, "Mosek fusion API for C++ version 9.0.86," 2019. [Online]. Available: https://www.mosek.com/downloads/9.0.86/

[36] M. B. Popovic, A. Goswami, and H. Herr, "Ground reference points in legged locomotion: Definitions, biological trajectories and control implications," *Int. J. Robot. Res.*, vol. 24, no. 12, pp. 1013–1032, Dec. 2005.

[37] J. Mao, J. Yang, X. Liu, S. Li, and Q. Li, "Modeling and robust continuous TSM control for an inertially stabilized platform with couplings," *IEEE Trans. Control Syst. Technol.*, vol. 28, no. 6, pp. 2548–2555, Nov. 2020.

[38] N. G. Tsagarakis, S. Morfey, G. M. Cerda, L. Zhibin, and D. G. Caldwell, "Compliant humanoid COMAN: Optimal joint stiffness tuning for modal frequency control," in *Proc. IEEE Int. Conf. Robot. Autom.*, 2013, pp. 673–678.

[39] Ubtech robotics corporation, [Online]. Available: https://www.ubtrobot.com/cn/

[40] Z.-Q. Luo, W.-K. Ma, A. M.-C. So, Y. Ye, and S. Zhang, "Semidefinite relaxation of quadratic optimization problems," *IEEE Signal Process. Mag.*, vol. 27, no. 3, pp. 20–34, May 2010.

Jiatao Ding (Member, IEEE) received the B.Eng. and Ph.D. degrees in engineering from Wuhan University, Wuhan, China, in 2014 and 2020, respectively.

From 2018 to 2020, he was a Visiting Ph.D. Student with the Italian Institute of Technology, Genoa, Italy. He is currently a Postdoctoral Researcher with the Department of Cognitive Robotics, 3mE, Delft University of Technology, The Netherlands. His research interests include legged locomotion, robot learning and model predictive control.

Linyan Han received the M.Sc. degree in control theory and control engineering from the Nanjing University of Aeronautics and Astronautics, Nanjing, China, in 2017. She is currently working toward the Ph.D degree in automation science with the School of Automation, Southeast University, Nanjing, China.

Her research interests include force control, position control, nonlinear control theory and their applications to robotic systems.

Ligang Ge received the B.Eng. and M.Sc. degrees in engineering from the National University of Defense Technology, Changsha, China, in 2014 and 2016, respectively.

He is currently a Senior Engineer with UBTECH Robotics Corporation, Guangdong, China. His research interests include gait generation for biped robot and balance control.

Yizhang Liu received the B.Eng. and M.Sc. degrees in engineering from the National University of Defense Technology, Changsha, in 2009 and 2015, respectively.

He is currently a Senior Engineer with UBTECH Robotics Corporation, Guangdong, China. His research interests include multijoints legged robot and manipulator control.

Jianxin Pang received the B.Eng. and Ph.D. degrees in engineering from the University of Science and Technology of China, Hefei, China, in 2002 and 2008, respectively.

He is currently the Director of UBTECH Research Institute, Guangdong, China and a Senior Engineer with UBTECH Robotics Corporation, Guangdong, China. His research interests include optimal control, machine learning, motion planning and their applications to humanoid robots, rescue robots, home service robots, and teaching robots.